

### Nanoscale

# HKUST-1 MOF Nanoparticles: Non-classical Crystallization Route in Supercritical CO2

Journal:	Nanoscale			
Manuscript ID	NR-COM-07-2024-003070.R1			
Article Type:	Communication			
Date Submitted by the Author:	12-Oct-2024			
Complete List of Authors:	Feng, Ji; University of Washington, Mechanical Engineering Lau, Almond; University of Washington, Mechanical Engineering Novosselov, Igor; University of Washington, Mechanical Engineering; University of Washington			

SCHOLARONE™ Manuscripts

### **COMMUNICATION**

## HKUST-1 MOF Nanoparticles: Non-classical Crystallization Route in Supercritical CO₂<sup>†</sup>

Received 00th January 20xx, Accepted 00th January 20xx

Ji Fenga, Almond Laua, and Igor V. Novosselov\*a

DOI: 10.1039/x0xx00000x

Reducing MOF particles to the nanoscale size range is beneficial due to their increased surface-to-volume ratio, higher defects exposing metals and ligands, and short diffusion path. While great efforts have been made to reduce the particle sizes by controlling the reaction kinetics or terminating the particle growth, largescale, rapid synthesis of MOF nanoparticles (NPs) remains a challenge. Here, we report supercritical (sc) CO2-assisted synthesis of HKUST-1 NPs in a continuous flow reactor, which yielded pure and thermally stable MOFs with median sizes of 110 - 250 nm and BET surface area of  $1610-1890 \ m^2/g$  with under 10 seconds synthesis time. ScCO2 and ethanol with a mole ratio of 9:1 are used as co-solvents for the fast nucleation of HKUST-1 and crystal formation. A typical dry yield of 53.7 wt % is achieved with 0.1 M Cu precursor under mild conditions at 75°C and 13 MPa. The space-time yields and surface area production rates are 5668 kg·m<sup>-3</sup>·d<sup>-1</sup> and 1.0\*10<sup>10</sup> m<sup>2</sup>·m<sup>-3</sup>·d<sup>-1</sup>. Particle size and morphology analysis indicate aggregation of nascent structures occurs in the aerosolized state, leading to a non-classical crystal growth mechanism and enabling multiple pathways for tuning the synthesis process. With the ability to recycle CO2, solvents, and unreacted precursors, the method can be used for the scalable production of MOFs.

#### 1. Introduction

The scalable and sustainable production of nanometer-sized, high-quality metal-organic frameworks (MOFs) is essential for bridging the gap between lab-scale research and real-world applications.<sup>1, 2</sup> Advancements in nanotechnology have led to the development of materials with properties that are superior to those of their bulk analogues. Metal-organic frameworks (MOF) nanoparticles (NPs) show enhanced catalytic performances due to the large number of

<sup>o</sup>Department of Mechanical Engineering and Institute for Nano-Engineered Systems, University of Washington, Seattle, WA 98195, USA

surface active centers.3 The fast transport of mass, ions, and electrons improves MOF performance and increases the cycling stability in energy storage applications.4 The dispersion properties, immune compatibility, and low toxicity of MOFs enable their application in drug delivery.5 Significant efforts have been made to synthesize MOF NPs directly through two primary methods: (i) controlling the crystal growth by promoting fast nucleation and slowing crystal growth or (ii) terminating crystal growth with amendments.<sup>6</sup> Rapid nucleation typically requires external energy sources, such as microwave irradiation and ultrasound.7, 8 Slow growth can be achieved by reducing the temperature and limiting the reaction time; however, this strategy can lead to poorly formed crystals and low yields. Applying surfactants and coordination modulators requires precise stoichiometric control of additives and MOF precursors, making it hard to implement in large-scale systems due to the spatial and temporal gradient and mixing limitation.<sup>2,9,10</sup> Transitioning from laboratory discoveries to practical applications requires high-yield, scalable production of high-quality MOF NPs, marking it a significant and actively explored research frontier. Continuous processes, including flow reactors, 11 microwaveassisted synthesis, 12, 13 microfluidic methods, 14 and spray-drying, 15 can provide environments that are not achievable in batch synthesis and are promising methods for large-scale MOF production.<sup>16</sup> We have reported the rapid MOF synthesis in a continuous flow reactor with supercritical CO2 (scCO2) as the reaction medium.<sup>17, 18</sup> ScCO<sub>2</sub> offers the benefits of both gas- and liquid-like, providing excellent diffusion and solvent power ideal for industrial processes.<sup>19</sup> Its low supercritical temperature is advantageous for synthesizing thermally sensitive materials, making it a promising option for the scalable production of MOFs.<sup>20</sup> As an eco-friendly, non-toxic, and non-flammable solvent, scCO2 can be recycled from industrial emissions, eliminating harmful organic solvents and reducing environmental impact.<sup>21</sup> These features make scCO<sub>2</sub> a sustainable choice for green chemistry and large-scale applications. ScCO2 has been reported to enable the formation of nanoparticles through a rapid expansion of scCO2 solution (RESS) and scCO<sub>2</sub> anti-solvent process (SAS).<sup>22</sup> Because of the low solubility of large solvent molecules and polar species in scCO<sub>2</sub>, studies have

<sup>\*</sup>Email address of the corresponding author: ivn@uw.edu.

<sup>†</sup>Supplementary Information available: [details of any supplementary information available should be included here]. See DOI: 10.1039/x0xx00000x

**Table 1.** Residence times in the reactor section for each set of HKUST-1 synthesis parameters. Subscripts indicate (1) the use of  $CO_2$ ethanol mixture densities from literature or (2) the use of pure  $CO_2$  and pure ethanol densities to estimate mixture densities.

Pressure, MPa	T, °C	$X_{EtOH}$ , mol/mol	Phase	$ au_{ m res,1}$ , s	$ au_{ m res,2}$ , s	
10	35	0.101	Single, liquid-like	12.40	12.41	
13	70	0.100	Single, gas-like	9.73	6.83	
10	70	0.101	Binary, gas-expanded liquid	6.32	4.76	

mainly focused on activating the MOF pores rather than the synthesis.<sup>23-25</sup> Only a few batch studies report the use of scCO<sub>2</sub> as a solvent in MOF synthesis.<sup>26-29</sup> Adding scCO<sub>2</sub> can provide a homogeneous reaction medium and minimize the use of organic solvents and additives. The solubility of the metal precursors and the organic linkers was increased by using fluorinated metal complexes or incorporating dioxane and ethanol as co-solvents. However, in those batch processes, MOFs formed over several hours.

This work describes the rapid synthesis (~10 sec) of MOF NPs in a continuous flow scCO<sub>2</sub>/EtOH co-solvent system, demonstrating the feasibility of high-yield, high-quality MOF production. HKUST-1, a 3D assembly of copper and trimesic acid (BTC) has been widely studied since its first discovery by Chui et al. 30-33 The Cu(II) ions with coordinatively unsaturated sites in HKUST-1 provide redox activity and Lewis acidity, making it a potential catalyst/support. It excels in gas adsorption and ionic/electrical conduction.  $^{\rm 34}$  In biomedical applications, the high porosity and surface area of HKUST-1 enable effective drug loading and controlled release, as seen with rifampicin, ibuprofen, and thymol.35-37 The release of Cu2+ under acidic conditions gives HKUST-1 antitumor and antibacterial properties, making it a versatile platform for chemotherapy, photodynamic, photothermal therapies, and wound healing.<sup>38</sup> If HKUST-1 is synthesized using scCO<sub>2</sub> as a solvent swelling agent and combined with dimethylformamide (DMF), a hierarchical pore structure can form due to particle assembly.<sup>39</sup> Furthermore, the influence of scCO<sub>2</sub> is evident in the development of additional porosity structures in HKUST-1 microcrystals following prolonged incubation. 40,41 This was attributed to acid etching. However, the

role of scCO<sub>2</sub> in the continuous flow synthesis and the mechanistic understanding of the rapid MOF synthesis are unclear.

In our study, ethanol was chosen as the co-solvent because of its high solubility to both  $Cu(NO_3)_2$  and BTC, as well as its ability to promote the rapid precipitation of HKUST-1.<sup>31, 42</sup> Other advantages of using ethanol are the low toxicity and high miscibility with scCO<sub>2</sub>, allowing us to reach supercritical conditions under mild conditions (< 100 °C, < 35 MPa), e.g., the critical point of  $CO_2$  / EtOH mixture ( $X_{EtOH}$  = 0.1) is ~ 50 °C and 9.6 MPa.<sup>43-45</sup> A comparative analysis of particle sizes, morphologies, and crystal structures as a function of operating conditions points to the aerosol-based MOF NP synthesis through particle aggregation and a non-classical crystallization route, enabling multiple pathways for tuning the synthesis process.

#### 2. Results

#### 2.1. Synthesis of HKUST-1 in a continuous flow reactor

HKUST-1 synthesis was performed in a modified counter-current continuous flow reactor, as detailed in Rasmussen et al.  $^{18}$  In a typical experiment (Fig. 1), CO $_2$  from the gas cylinder is cooled to liquid T  $^{\circ}$  0 °C, as measured by a thermocouple (TC 1, type K, Omega Engineering, Inc., Norwalk, CT, USA) in a calcium chloride bath and pumped (Model 305 HPLC Pump, Gilson, Middleton, WI, USA) into the reactor at a controlled flow rate (up to 25 ml/min). The CO $_2$  stream is heated to a supercritical phase by a cartridge heater (800 W, 120 V, Tempco Electric Heater Corporation, Wood Dale, IL, USA) before entering the counterflow reactor section. The precursors are pumped (Model 515 HPLC Pump, Waters Corporation, Milford, MA, USA) in two separate lines that merge before entering the counter-current reactor (Internal Vo = 3.95 mL).

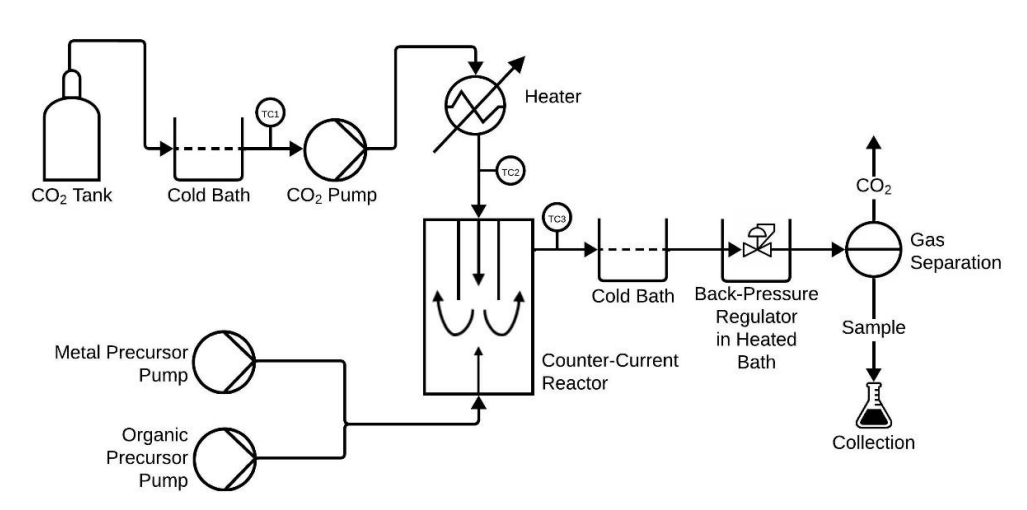


**Fig. 1** Counter-current continuous flow synthesis reactor with K-type thermocouples (TC) measures the fluid temperature, and a back pressure regulator (BPR) maintains the system pressure.

**Journal Name** COMMUNICATION

The mixture enters an insulated 316 stainless steel (SS) tubing (V = 3.22 mL) through a cold bath and exits through a back pressure regulator (BPR) (Model B6R, Equilibar, LLC, Fletcher, NC, USA) placed in a heated bath to prevent CO<sub>2</sub> transition to dry ice and clogging the reactor. The effluent is collected in glass bottle, and the CO2 is separated naturally. The pressure is set by the BPR (10 MPa or 13 MPa), and the reactor fluid temperature (TC 3) is controlled by the proportional-integral-derivative (PID) controller (Model TPC10008, Tempco Electric Heater Corporation). Clean ethanol at room temperature (T = 20-25 °C) is injected until the steady-state condition is achieved at precursor flow rates 1.8 mL/min through each pump or 0.1 mole fraction of EtOH to a 0.9 mole fraction of CO<sub>2</sub> (25 mL/ min). Once a steady state was achieved, the neat EtOH injection was switched to the HKUST-1 precursor/EtOH solutions, and sample collection began after HKUST-1 formation was observed in the effluent. Fig. S6. shows the reactor setup.

#### 2.2. Residence time calculation

The residence times  $(\tau)$  for each reaction condition were calculated using Equation (1):

$$\tau_{res} = \frac{\rho V}{m} , \qquad (1)$$

 $\tau_{res}=\frac{\rho V}{\dot{m}}\;, \tag{1}$  where V is the volume of the reactor,  $\dot{m}$  is the mass flow rate of the

 $CO_2/EtOH$  mixture, and  $\rho$  is the estimated density of the mixture corresponding to TC3 measurement (placed inside the reactor), set pressure, and the EtOH mole fraction in CO2. Although there are published data on mixture densities for the CO<sub>2</sub>/EtOH binary phase system, these data do not cover the wide range of possible mixture pressure, temperature, and concentration combinations. Additionally, most available mixture densities encompass mixtures at either liquid or gaseous phase saturation, excluding points within the two-phase region. Therefore, two methods were employed to estimate  $\rho$  corresponding to our experimental conditions: (1) approximation based on the existing literature values<sup>46-48</sup> via interpolation and extrapolation, (2) weighted average of the mass fractions of each compound based on the densities of pure CO249,50 and of pure ethanol 51,52 at the various temperatures and pressures. The metal and organic precursors were assumed to have negligible impact on the mixture density. Table 1 shows the residence times for the reactor section, including the insulated tubing section up to the cooling bath.

#### 2.3. Morphology and size analysis

Though the reaction process is evidently different from traditional MOF synthesis, the method yielded high-quality MOF NPs in ~ 10 s in all experiments. To understand the particle growth mechanism

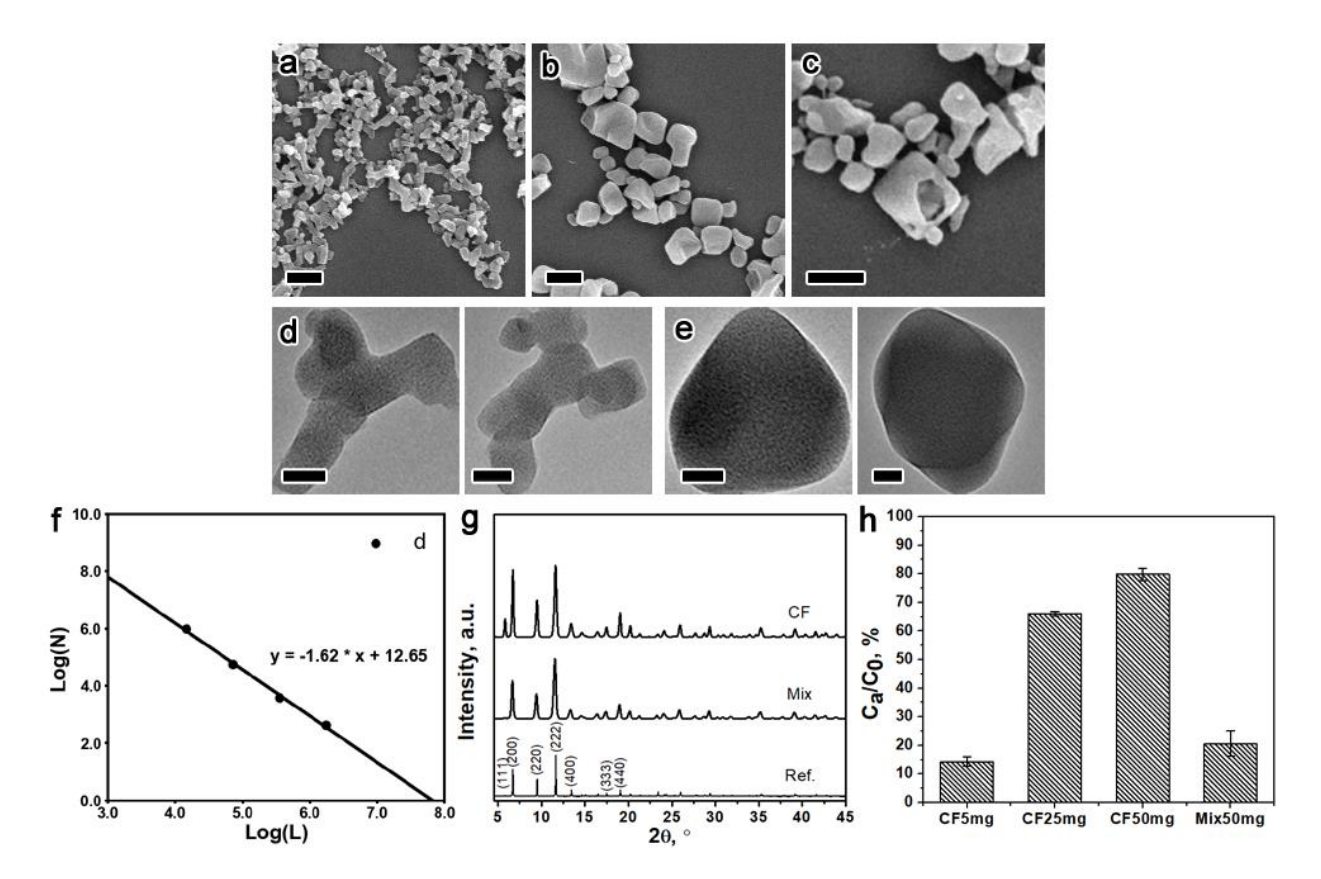


Fig. 2 SEM and TEM images of particles obtained by mixing in pure ethanol (Mix, a, d) and continuous flow synthesis with scCO<sub>2</sub> (CF, X<sub>EtOH</sub> = 0.1, b, c, and e). The scale bars in the SEM images are 500 nm (a-c), and 50 nm in TEM Images (d, e). Plot (f) 2dimensional fractal analysis of typical morphologies in d, where N and L represent the number of boxes used to cover the particle and the length of the box in pixel sizes. The inset equations show the linear fit results, with the negative value of the slope indicating the fractal dimension. (g) XRD pattern of the reference, and the Mix and CF products in the absence and presence of scCO<sub>2</sub>. (h) Adsorption of Ibuprofen using non-activated CF and Mix samples.

**Table 2.** Summary of particle size analysis and BET surface area for the  $scCO_2$ -assisted synthesis at 75°C and 13 MPa.

[Cu(NO <sub>3</sub> ) <sub>2</sub> ]	0.01 M	0.05 M	0.1 M	0.3 M
Size <sub>mean</sub> , nm	110.25	128.39	139.53	214.64
SD, nm	56.61	80.54	84.66	124.88
$r_1^a$ , nm	55.46	67.96	67.30	98.09
$r_3$ <sup>b</sup> , nm	71.64	91.47	85.71	120.33
$r_h^c$ , nm	43.92	49.38	51.54	75.89
$\mu_1$	1.63	1.85	1.66	1.58
$\mu_3$	0.77	0.74	0.78	0.82
$PDI^d$	0.51	0.61	0.63	0.58
BET surface area,				
m²/g	_e	1845	1766	1895

 ${}^{a}r_{1} = \sum r_{i}/N; {}^{b}r_{3} = \sqrt[3]{\sum r_{i}^{3}/N}; {}^{c}r_{h} = N/\sum(1/r_{i});$ 

<sup>d</sup>PDI = SD/Size<sub>mean</sub>. <sup>e</sup>Not performed due to low production rate.

and illustrate the impact of  $scCO_2$ , we first compare the products obtained in the absence and the presence of  $scCO_2$ . The former was synthesized by mixing 0.3 M  $Cu(NO_3)_2$  and 0.24 M BTC ethanolic solutions. The products were centrifuged immediately after mixing to match the reaction time of the  $scCO_2$ -assisted case. The latter was performed in the continuous flow reactor with  $scCO_2$  at 35 °C and 10 MPa; the lower temperature could not be tested due to the proximity to the critical point. The two ethanolic precursors initially encounter each other at near room temperature, followed by mixing with  $scCO_2$ .

ScCO $_2$  facilitates the formation of HKUST-1 particles with clean pores. Small particle aggregates were formed in the ethanol rapid-mixing case without scCO $_2$  (Fig. 2a). TEM images (Fig. 2d) show nascent crystals (~ 30 nm) interconnecting to form "worm-like" structures. This observation aligns with existing literature indicating that HKUST-1 particles precipitate rapidly due to the limited interaction between ethanol and BTC, forming low-quality crystals with a low surface area (~840 m²/g). $^{53}$  In the scCO $_2$ -assisted synthesis, we observed larger particles, hollow structures, and irregularly shaped particles - "broken crystals" (Fig. 2b and c). To further characterize the morphology of the products, we conducted a 2-D fractal analysis on five randomly chosen particle aggregates for the ethanol rapid mixing case.  $^{54,55}$ 

Fractal analysis has been widely used as a key parameter to describe the fractal morphology of aerosol aggregate particles.<sup>56</sup> Fractal dimension measures complexity related to key features of fractals, such as self-similarity or degree of irregularity. Each aggregate was imaged using a 2048\*2048 square grid and divided by boxes with sizes (L) of 64, 128, 256, and 512 pixels. The number of boxes that cover the particle was denoted as N. Fig. 2f shows the data points of log(N)/log(L) and the linear fit for one fractal. The averaged fractal dimension was calculated to be 1.65 for the ethanol rapid mixing case, which aligns with the fractal dimension of "worm-like" particles observed during the early stages of nonclassical nucleation, as reported in Kumar et al. 55 However, after exposure to scCO<sub>2</sub>, the particles lost their fractal nature (Fig. 2e), indicating extensive crystal reorganization in the presence of scCO<sub>2</sub>. Both samples (Fig. 2g) show typical diffraction peaks of the HKUST-1 phase in comparison to the reference. 57 For the sample synthesized in the scCO<sub>2</sub>/EtOH mixture (CF), the (111) peak indicates the

absence of solvent molecules in the HKUST-1 pores.  $^{58,59}$  The highly accessible pores contribute to a high BET surface area of 1887 m²/g. The high ratio of  $I_{(200)/}I_{(220)}$  suggests a low hydration degree of the product.  $^{15, 32, 60}$  The clean pores of the CF HKUST-1 facilitate the adsorption of molecules without the need for the additional activation steps. In our adsorption experiments with a 0.5 mg/mL ibuprofen (IBU) solution (Fig. 2h), the CF HKUST-1 at 5, 25, and 50 mg adsorbed 14%, 66%, and 80% of the initial IBU concentration, respectively. In contrast, 50 mg of the Mix HKUST-1 sample only achieved 20 % adsorption.

The significant morphological difference, shown in Fig. 2d and e, points to a difference in particle growth pathway. Two general crystal growth mechanisms can be considered: (i) classical growth, involving the layer-by-layer deposition of monomer on the surface of the crystals; (ii) non-classical growth, characterized by the attachment of several precursor types (amorphous or small crystals with different sizes in either solid, liquid, or gas-like state), followed by morphology reshaping due to Ostwald ripening. 61-63 MOF synthesis was traditionally explained by the classical crystal growth process, with only a few reports describing the non-classical growth in the solution phase. Liu et al. used cryo-TEM to characterize the intermediate structures during the growth of ZIF-8, revealing crystallization within amorphous clusters in the solute-rich liquid phase.<sup>64</sup> Kumar et al. show that aggregation of nuclei gives rise to 2D structures at the early stage of the reaction, which then undergoes ripening to yield high-dimensional structures. 55

In our case, the co-existence of both large and small particles, accompanied by hollow structures (Fig. 2c), cannot be explained by classical growth. Additionally, the crystal domain size of HKUST-1 synthesized in the  $scCO_2$ /ethanol mixture is only ~ 30.0 nm, much smaller than the particle size. The crystal domain size was determined using the Scherrer equation, based on the most intense (222) peak observed in the XRD pattern (Fig. 2g):  $^{65-68}$ 

$$crystal\ domain\ size = \frac{\kappa\lambda}{\beta cos(\theta)},$$

where K is the shape factor (0.9 from literature<sup>66, 69, 70</sup>),  $\lambda$  is the X-ray wavelength of Cu (1.5406 Å),  $\theta$  is the line broadening at half the maximum intensity, and  $\vartheta$  is the Bragg angle. The polycrystalline nature of the MOF particles produced in the scCO<sub>2</sub> supports the hypothesis of MOF particle growth via aggregation of nascent particles. The interaction of the particles in the environment has been extensively studied in the formation of carbonaceous aerosol aggregates in flames. However, the strict definition of aerosol synthesis does not necessarily apply to MOF NP growth on scCO<sub>2</sub> for two reasons: (i) the particles are suspended in the supercritical fluid, which can be fluid- or gas-like depending on the operating temperature and pressure, i.e., left or right from the Widom line in the single-phase scenarios, (ii) the mixture phase was varied in the experiments, in some cases the synthesis was performed in two-phase EtOH(liquid)/scCO<sub>2</sub> system.

SEM images for different concentrations of Cu(NO<sub>3</sub>)<sub>2</sub>: 0.01 M (b), 0.05 M (d), 0.1 M (e), and 0.3 M (f). (c) TEM image of products obtained with 0.01 M of Cu(NO<sub>3</sub>)<sub>2</sub>. All the synthesis was performed at  $X_{EtOH} = 0.1$ , T = 75 °C, P = 13 MPa. The scale bars are 100 nm in (c) and 500 nm in the rest.

Journal Name COMMUNICATION

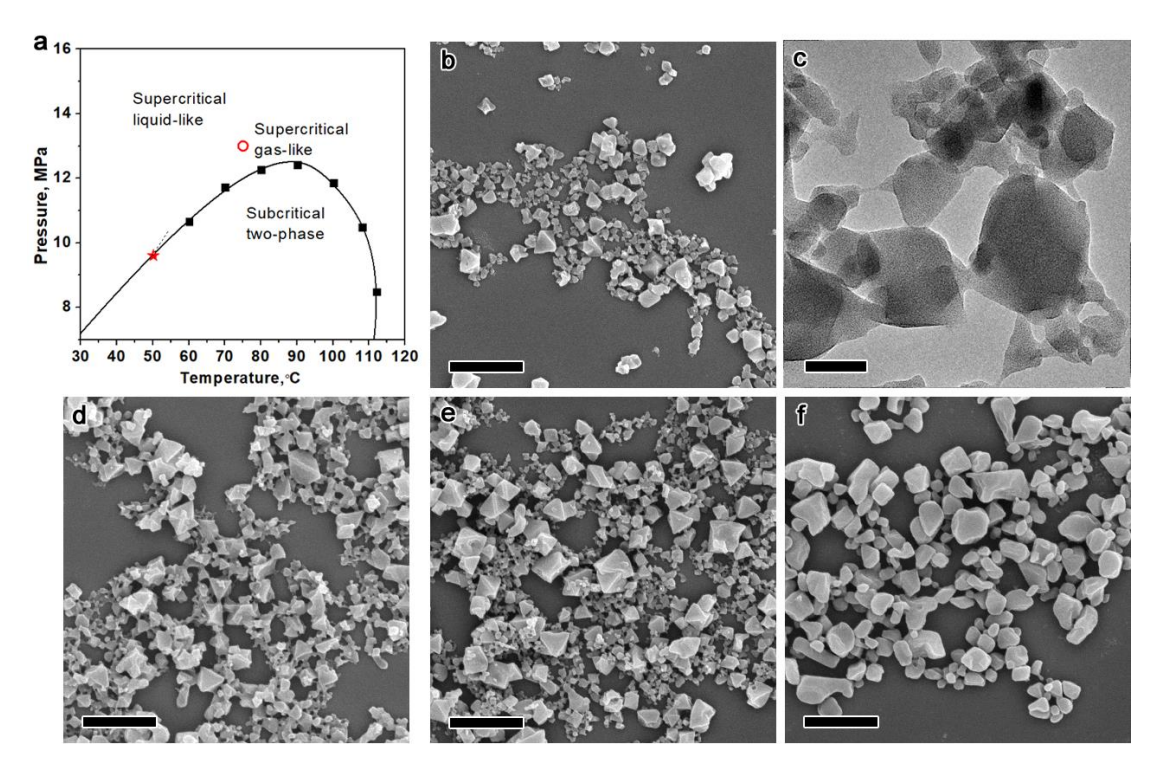


**Fig. 3** (a) Phase diagram of the ethanol and  $scCO_2$  mixture ( $X_{EtOH} = 0.1$ ). The star and hollow circle indicate the critical point and the reaction condition. The dashed line is the estimated Widom line. SEM images for different concentrations of  $Cu(NO_3)_2$ : 0.01 M (b), 0.05 M (d), 0.1 M (e), and 0.3 M (f). (c) TEM image of products obtained with 0.01 M of  $Cu(NO_3)_2$ . All the synthesis was performed at  $X_{EtOH} = 0.1$ , T = 75 °C, P = 13 MPa. The scale bars are 100 nm in (c) and 500 nm in the rest.

Fig. 3a plots the phase diagram of the EtOH/  $CO_2$  with  $X_{EtOH} = 0.1$ using data from references.44 The estimation of the Widom line is difficult for a two-phase mixture. It is generally plotted as a tangent line at the critical point. Critical point for a two-phase system can be obtained experimentally.45 To probe the aerosol-like assembly mechanism, the system was operated in a single-phase region where EtOH is fully miscible with the scCO<sub>2</sub> in a gas-like region (Fig. 3a, circle). The Cu(NO<sub>3</sub>)<sub>2</sub> availability was varied between 0.01 to 0.3 M to change the number of nucleation sites. BTC was in excess in all cases, making Cu<sup>2+</sup> ions the limiting reagents. Pure HKUST-1 particles were produced with a high BET surface area above 1750  $m^2/g$  (Fig. 4b and Table S2). In a case at 0.1 M  $Cu^{2+}$  ions at  $75\ ^{\circ}\text{C}$  under 13 MPa, the synthesis had a dry yield of 53.7 wt% ( $yield\% = \frac{\textit{Actual yield}}{\textit{Theoretical yield}}*100\%$ ). The space-time yields (STY, kg product/ m³ reactor volume/ day) and surface area production m<sup>2</sup> BET surface area/ m<sup>3</sup> reactor/ day) (SAPRs, 5668 kg·m $^{-3}$ ·d $^{-1}$  and 1.0\*10 $^{10}$  m $^{2}$ ·m $^{-3}$ ·d $^{-1}$ . Compared to other continuous synthesis reports for HKUST-1, our approach (i) achieves a short residence time of less than 10 s, enabling high-throughput production; (ii) produces nanoparticles with a large BET surface area, making them promising for applications like gas adsorption and drug delivery; (iii) utilizes a compact reactor with a reaction volume of 3.22 cm<sup>3</sup> (that can be readily scaled), without the need for additional equipment such as a microwave generator, making it easy to scale up for real-world applications; and (iv) employs scCO<sub>2</sub> and a small amount of ethanol, avoiding the use of high-boilingpoint and toxic chemicals, ensuring a green and sustainable synthesis process.

The particle size distribution in the yield was examined through SEM images (Fig. 3b - e). Both large and small particles are present in each image. A change in morphology and particle size distribution is observed with an increase in  $\text{Cu}(\text{NO}_3)_2$  concentration. For 0.01 M  $\text{Cu}(\text{NO}_3)_2$ , the predominant MOF particles measure 30 - 50 nm, and a small percentage exhibit octahedral morphology (Fig. 3b and c). Increasing the concentration of  $\text{Cu}(\text{NO}_3)_2$  to 0.1 M yielded more octahedral structures (Fig. 3d). When the concentration of  $\text{Cu}(\text{NO}_3)_2$  was increased to 0.3 M (near stoichiometric), the MOF crystals lost the octahedral shape, becoming more spheroidal (Fig. 3e).

The particle size distribution (Fig. 4a) was plotted by measuring ~400 particles from the SEM images. The long tail of the lognormal distribution indicates the aggregation-induced broadening of particle size distribution. The red curves show a lognormal fit with

the equation:  $y=y_0+\frac{A}{\sqrt{2\pi}wx}e^{\frac{-(\ln\frac{x}{X_c})^2}{2w^2}}$ , where  $x_c$  and w correspond to the center and log standard deviation of the distribution, respectively. These values were used to calculate the mean particle size and polydispersity index (PDI). The mean particle size was calculated as  $r_{mean}=x_ce^{\frac{w^2}{2}}$ . The mean particle size increased from 110 to 215 nm at higher Cu²+ concentrations. To evaluate the crystal growth mechanism, the moments of the size distribution were calculated as  $\mu_1=r_3/r_h$  and  $\mu_3=r_1/r_3$ , where  $r_1,r_3$ , and  $r_h$  are the arithmetic mean radius, cube mean radius, and harmonic mean radius. Both moments are close to unity for monodisperse

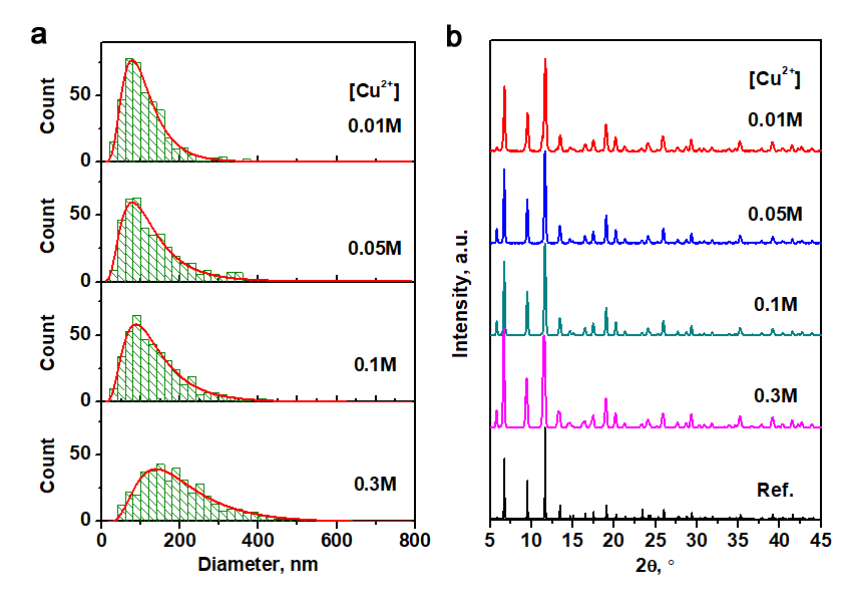


Fig. 4 Particle size distribution (a) and XRD spectra (b) of products obtained with different concentrations of Cu(NO<sub>3</sub>)<sub>2</sub>. All the synthesis was performed in  $X_{EIOH} = 0.1$ , T = 75 °C, P = 13 MPa.

particles formed through classical nucleation and growth. <sup>71-73</sup> Table 2 shows  $\mu_{I} > 1.25$  and  $\mu_{3} < 0.905$ , suggesting that the crystal growth in our experiments occurs through particle aggregation.

#### 2.4. Formation mechanism of HKUST-1 nanoparticles

Fig. 5 illustrates the proposed particle growth mechanism. The nascent 20-50 nm cubic-like crystals are formed by rapid aggregation into "worm-like" structures. This process occurs in the EtOH solution immediately upon mixing Cu<sup>2+</sup> ions and BTC (Fig. 2d). Upon entering the scCO<sub>2</sub>, the solvent EtOH and precursors become miscible with CO<sub>2</sub>, and the further interaction between the nascent particle aggregates and the available precursors occurs in an aerosol-like manner.

Consider gas-like single-phase condition (P = 13 MPa,  $T = 75 \,^{\circ}\text{C}$ , Table 1 and Fig. 3a), where upon mixing with  $\text{scCO}_2$ , the nascent particles become aerosolized in a mixture of  $\text{scCO}_2$  and unreacted precursors. In the gas-like  $\text{scCO}_2$  phase and turbulent flow conditions, the reagent mixing is not likely to be a limiting factor in reaction kinetics. Overcoming Brownian diffusion limits of the batch reactors, the continuous flow supercritical fluid systems benefit from the fast mass transport due to rapid mixing and miscibility of

the reagents, leading to fast reactions.74-77 Nascent particles act as heterogeneous nucleation sites. Two growth pathways can be considered: (1) particle-particle assembly, where particles aggregate, forming "Tetris-like" compact structures, and (2) vapor deposition, where ions and amorphous oligomers self-assemble in the nascent aggregates, filling up the hollow structures in the aggregates. These routes are not self-exclusive and are likely present for all conditions. A low concentration of nucleation sites and a high concentration of unreacted reagents favor route 2. The presence of liquids in a two-phase scCO<sub>2</sub>/solvent mixture will also be conducive to this route. In contrast, if a large number of nanocrystals are formed rapidly, depleting the precursor pool, the aggregates will form primarily by particle collision, i.e., route 1. On particle collision: Particle collision rates in laminar shear flow were proposed by Smoluchowski,78 and the enhancement of the collision rate by turbulence was described by Saffman & Turner in 1956.79 Since then, the phenomena have been observed in multiple

scenarios from cloud formation to carbon soot growth. In our

systems, the reactor's Reynolds (Re) number exceeds the turbulent

transition criteria, Re~13,000 (based on the jet diameter) at

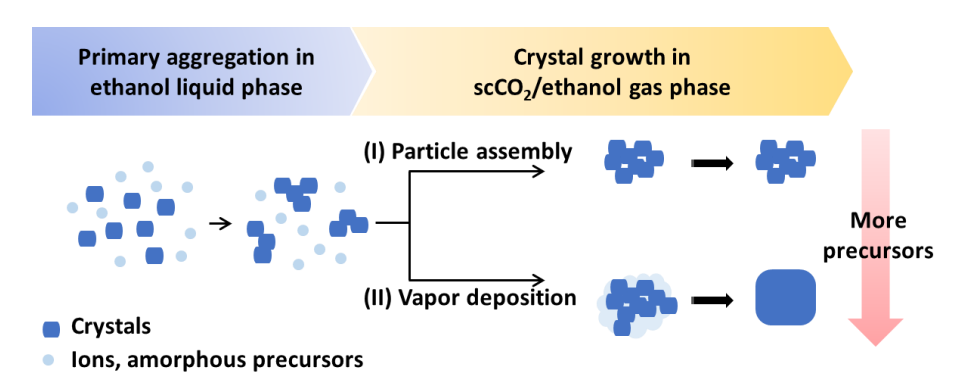


Fig. 5 Schematic illustration of the non-classical particle growth.

Journal Name COMMUNICATION

T = 75°C, P = 13 MPa conditions. Counterflow mixing (Fig. 1) provides high shear stress conditions for rapid EtOH atomization and transition to a single-phase reaction environment.<sup>17, 18</sup> The physical properties of scCO<sub>2</sub> enhance solid particle interaction upon initial contact. The low dielectric constant of scCO2 screens electrostatic repulsion,80 allowing the van der Waals force to dominate particle-particle interaction. Fig. 3c shows aggregates produced at the lowest concentration of the Cu<sup>2+</sup> precursor, i.e., the lowest available number of nucleation sites. Collision rates can be estimated as  $N=\alpha n^2$ , where  $(\alpha)$  is a collision frequency coefficient, which would not significantly vary with initial concentrations of Cu2+, assuming uniformity among nascent particles, and the particle number concentration (n).<sup>81</sup> The increase in particle size at higher Cu<sup>2+</sup> concentrations can be attributed to the high collision rates between the nascent particles and the consequential crystal restructuring.On particle growth: Nonclassical growth can be promoted by assembling amorphous or crystal structures, liquid- or gas-like precursors, followed by recrystallization due to Ostwald ripening. The initial aggregates can be subjected to precursor coating or matrix filling, where vapors of ions and amorphous oligomers self-assemble in the nascent aggregates. This scenario can be compared with well-studied carbon soot formation mechanisms, specifically cases with long residence time and complex exposure to precursor-rich regions where the nanoparticle aggregates have extended interaction with molecular precursors.82 Analogous to the scCO2 MOF synthesis, bridging and gap filling between the individual carbon particles in the aggregate occurs by depositing organic carbon over the existing aggregates during their repeated exposure to organic precursors.83 Contrasting the MOFs' nanostructure, the mature carbon particles (20-100 nm) consist of closed graphene layers forming onion-like structures; they assemble into branching aggregates with minimal particle-particle interaction and, with a given long residence time, could form carbon aerogels.84 MOF nanocrystals have cube-like morphology, and particles coagulate, forming "Tetris-like" structures with strong interaction between the facets. Based on the Scherrer equation, the resulting polycrystalline structures are ~ 50-500 nm with a crystal domain size of ~30.0 nm. During this assembly, the particles lose their initial fractal nature, and the final product shows hollow structures and irregularly shaped particles -"broken crystals" (Fig. 2b and c).

Two-phase system: This non-classical growth mechanism applies to synthesis in the EtOH(liquid)/scCO<sub>2</sub> two-phase scenario. Decreasing the reaction pressure to 10 MPa leads to more spheroidal particles (Fig. S1), characterized by a broad particle size distribution (Fig. S2). The size distribution moments fall within the regime of  $\mu_1 > 1.25$ and  $\mu_3$  < 0.905 (Table S1), which sets apart the particle formation process from classical growth mechanisms. In contrast to the single gas phase, the liquid-in-gas phase has interfaces such as bubbles or droplets. The limited mixing within this two-phase environment adds complexity to particle-particle interactions. The particle can enter the liquid and scCO<sub>2</sub> phase repeatedly. In this process, the precursors can be deposited on the particle in the liquid phase and recrystallized in the scCO<sub>2</sub>. The process is less controlled; however, the BET surface area is not influenced by the particle size or synthesis method (Table S2), and the PXRD shows no significant differences in the MOF crystal structure (Fig S3). The analysis confirms that the presence of scCO<sub>2</sub> during the synthesis promotes high-quality HKUST-1 MOF nanoparticles.

To explore the potential applications for pharmaceutical delivery, we activated the HKUST-1 nanoparticles at 90°C overnight and then performed ibuprofen (IBU) adsorption experiments. Using a 3 mL IBU solution with an initial concentration of 5 mg/mL, we achieved adsorption capacities of 619, 401, 327, and 257 mg/g IBU for 5, 12.5, 25, and 50 mg of HKUST-1, respectively (Table S3). Compared with 340 mg/g IBU loading reported in the literature,<sup>37</sup> the loading capacities of our samples indicate the high quality of the HKUST-1 synthesized in scCO<sub>2</sub>, highlighting their potential for applications in the biomedical field.

#### 3. Conclusions

We present a mechanistic explanation of MOF nanoparticles synthesis continuous flow scCO2 environment. Operating in a singlephase region, we obtained high-quality HKUST-1 nanoparticles in the 110 - 250 nm range, with BET surface areas > 1700 m<sup>2</sup>/g. The formation of HKUST-1 nanoparticles follows a non-classical crystal growth mechanism, as evidenced by the presence of complex polycrystalline structures with cavities and other defects originated by the assembly process of nascent MOF aggregates. The roles of scCO2 in the synthesis can be summarized as follows: 1) the turbulent flow generated by scCO2 accelerates the collision of nascent nanoparticles; 2) the low dielectric constant of scCO<sub>2</sub> minimizes particle repulsion, facilitating coagulation, followed by particle ripening; 3) scCO<sub>2</sub> purges solvents and other impurities from the micropores, resulting in high surface areas without additional MOF activation procedures. A non-classical crystal growth mechanism observed with HKUST-1 NP may be a universal phenomenon in MOF synthesis in a well-mixed scCO<sub>2</sub> environment. Two routes for particle growth (particle assembly and vapor deposition) are proposed, which can readily be controlled by process parameters influencing particle morphologies without sacrificing MOF quality. Our insights could inform future designs of synthesis reactors and can be applied to syntheses of other MOF particles.

#### Materials and methods

#### Chemicals

All obtained chemical products were used in their supplied condition without additional purification. Copper (II) nitrate trihydrate ( $Cu(NO_3)_2 \cdot 3H_2O$ , 99%, Sigma-Aldrich, Darmstadt, Germany) of 0.01 - 0.3 M and benzene-1,3,5-tricarboxylic acid, (BTC, 95%, Sigma-Aldrich) of 0.24 M were dissolved in ethanol (200 Proof, Decon Labs, Inc., King of Prussia, PA, USA). Gas cylinders of carbon dioxide ( $CO_2$ , 99.5%, Linde, Danbury, CT, USA) were used to operate the reactor.

#### Sample collection

The samples were centrifuged (Eppendorf Centrifuge 5430) at 7830 rpm until a clear supernatant was observed, typically after 10-25 min, and washed with ethanol four times. The solid product was dried overnight in an oven at 70°C.

#### **MOF NP Characterization**

The product was characterized via powder x-ray diffraction (PXRD) (Bruker D8 Discover), equipped with a microfocus X-ray source and Pilatus 100K large-area 2D detector, operated at 50 kV and 1000 μA over an angular range of  $2\theta = 5 - 45^{\circ}$ . The particles' morphology was characterized using scanning electron microscopy (SEM, FEI Sirion XL30) at 5 kV. A drop of sample dispersed in ethanol was deposited onto an oxygen-plasma-cleaned silicon wafer and coated with ~4 nm of platinum using Leica EM ACE600. SEM images taken at 20,000x magnification were used to generate the size distribution with the help of ImageJ software. The crystal structure was also characterized using transmission electron microscopy (TEM, FEI Tecnai G2 F20 SuperTwin) operated at a 200 kV accelerating voltage. Thermal stability data was collected via TGA (Mettler Toledo TGA/DSC 3+) on ~4 mg of powder sample to obtain mass loss curves as temperature by 10 °C/min from room temperature to 550°C. BET surface area was determined using nitrogen sorption at 77 K with a Micromeritics 3Flex gas sorption analysis system. The samples were heated at 140 °C for 12 hours on Micromeritics Smart VacPrep to remove any adsorbed molecules before the analysis. The UV-vis spectra were recorded using a PerkinElmer Lambda 950 UV Vis/NIR spectrophotometer.

#### **IBU** adsorption

To estimate the amount of ibuprofen loaded onto the HKUST-1 nanoparticles, we generated a calibration curve using IBU solutions in hexane with known concentrations. Fig. S4 illustrates the UV-vis spectra for IBU concentrations ranging from 0.01 mg/mL to 0.05 mg/mL. The absorption intensity of the peak at 263 nm was plotted against the concentration, resulting in a linear relationship (as shown in Fig. S5).

For comparing the CF and Mix HKUST-1 samples, the solids were dried overnight at ambient conditions and then ground. We added 5, 25, and 50 mg of CF and 50 mg of Mix HKUST-1 to 3 mL of a 0.5 mg/mL ( $C_0$ ) IBU-hexane solution in glass vials. The mixtures were shaken for 3 hours and allowed to stand for 13 hours.

In the case of activated CF HKUST-1, the powders were dried at 90°C overnight before being mixed with 3 mL of a 5 mg/mL IBU solution.

The solutions were separated from the solids through centrifugation and then analyzed after dilution. The absorption spectra of the liquid were measured to calculate the equilibrium concentration (Ce, mg/mL). The adsorbed concentration was determined using the formula: Ca = Co-Ce. Finally, the adsorption capacity was calculated using the equation:  $q_e = \frac{C_0 - C_e}{...} \times (3 \, \mathrm{ml})$ .

#### **Author contributions**

Ji Feng designed the experiments and wrote the manuscript. Ji Feng and Almond Lau conducted all the experiments and analyzed the data. Igor V. Novosselov supervised this work and revised the manuscript.

#### Data availability

The authors confirm that the data supporting the findings of this study are available within the article and its supplementary

materials.

#### **Conflicts of interest**

There are no conflicts to declare.

#### Acknowledgements

This work was partly conducted at the Molecular Analysis Facility, a National Nanotechnology Coordinated Infrastructure (NNCI) site at the University of Washington. The facility is supported in part by funds from the National Science Foundation (awards NNCI-2025489, NNCI-1542101), the Molecular Engineering & Sciences Institute, and the Clean Energy Institute.

The authors thank Prof. Chris Sorensen of Kansas State University for his advice in fractal dimension analysis; UW Molecular Analysis Facility staff members Ellen Lavoie, Scott Braswell, and Samantha Young for their assistance with TEM, SEM, and PXRD; RTT staff member Michael De Siena for helping with particle separation; and Washington Clean Energy Testbeds research scientist Dr. Philip Cox for helping with BET. They also thank Ivan Boris for his help with nanoparticle size analysis and Teddy Lautch for his help with reactor operation.

#### **Notes and references**

- M. Ding, R. W. Flaig, H.-L. Jiang and O. M. Yaghi, Chem. Soc. Rev., 2019, 48, 2783-2828.
- N. Hanikel, M. S. Prévot and O. M. Yaghi, Nat. Nanotechnol., 2020, 15, 348-355.
- 3. J. Wang, I. Imaz and D. Maspoch, Small Struct., 2022, **3**, 2100126.
- P. Xiao, F. Bu, R. Zhao, M. F. Aly Aboud, I. Shakir and Y. Xu, ACS Nano, 2018, 12, 3947-3953.
- K. A. S. Usman, J. W. Maina, S. Seyedin, M. T. Conato, L. M. Payawan, L. F. Dumée and J. M. Razal, NPG Asia Mater., 2020, 12, 58.
- H. Bunzen, M. Grzywa, M. Hambach, S. Spirkl and D. Volkmer, Cryst. Growth Des., 2016, 16, 3190-3197.
- S. H. Jhung, J.-H. Lee, J. W. Yoon, C. Serre, G. Férey and J.-S. Chang, *Adv. Mater.*, 2007, 19, 121-124.
- L.-G. Qiu, Z.-Q. Li, Y. Wu, W. Wang, T. Xu and X. Jiang, Chem. Commun., 2008, DOI: 10.1039/B804126A, 3642-3644.
- 9. S. Rojas and P. Horcajada, *Chem. Rev.*, 2020, **120**, 8378-8415.
- E. Karbassiyazdi, M. Kasula, S. Modak, J. Pala, M. Kalantari, A. Altaee, M. R. Esfahani and A. Razmjou, *Chemosphere*, 2023, 311, 136933.
- 11. M. Rubio-Martinez, M. P. Batten, A. Polyzos, K.-C. Carey, J. I. Mardel, K.-S. Lim and M. R. Hill, *Sci. Rep.*, 2014, **4**, 5443.
- 12. M. Taddei, D. A. Steitz, J. A. van Bokhoven and M. Ranocchiari, *Chem. Eur. J.*, 2016, **22**, 3245-3249.
- C. McKinstry, E. J. Cussen, A. J. Fletcher, S. V. Patwardhan and J. Sefcik, J. Chem. Eng., 2017, 326, 570-577.
- 14. Y. Wang, L. Li, H. Liang, Y. Xing, L. Yan, P. Dai, X. Gu, G. Zhao and X. Zhao, *ACS Nano*, 2019, **13**, 2901-2912.
- X. He, Z. Gan, S. Fisenko, D. Wang, H. M. El-Kaderi and W.-N. Wang, ACS Appl. Mater. Interfaces, 2017, 9, 9688-9698.
- J. Sun, H. T. Kwon and H.-K. Jeong, *Polyhedron*, 2018, **153**, 226-233.

**Journal Name COMMUNICATION** 

- 17. E. G. Rasmussen, J. Kramlich and I. V. Novosselov, ACS Sustainable 48. M. P. Dirauf, M. Conrad and A. S. Braeuer, Fluid Phase Equilib., Chem. Eng., 2020, 8, 9680-9689.
- 18. E. G. Rasmussen, J. Kramlich and I. V. Novosselov, J. Chem. Eng., 2022, **450**, 138053.
- 19. Y. Medina-Gonzalez, S. Camy and J.-S. Condoret, ACS Sustainable 50. M. M. E. Lemmon, D. Friend, P. Linstrom, and W. Mallard, NIST Chem. Eng., 2014, 2, 2623-2636.
- 20. J. Shi, X. Kang, L. Mao, Y. Jiang, S. Zhao, Y. Liu, B. Zhai, H. Jin and L. 51. P. Ahmadi, B. N. Karim Nobakht and A. Chapoy, J. Chem. Eng. Guo, J. Chem. Eng., 2023, 459, 141608.
- A. Z. Chen, Sci. Technol. Adv. Mater., 2021, 22, 695-717.
- Soc., 2009, 131, 458-460.
- 24. Z. Xiang, D. Cao, X. Shao, W. Wang, J. Zhang and W. Wu, Chem. Eng. Sci., 2010, 65, 3140-3146.
- 25. M. F. Dapaah and B. Liu, J. Inorg. Organomet. Polym. Mater., 2020, 56. C. Oh and C. M. Sorensen, J. Colloid Interface Sci., 1997, 193, 17-30, 581-595.
- 26. A. López-Periago, O. Vallcorba, C. Frontera, C. Domingo and J. A. 57. Ayllón, Dalton Trans., 2015, 44, 7548-7553.
- 27. A. M. López-Periago, N. Portoles-Gil, P. López-Domínguez, J. Fraile, 58. J. Saurina, N. Aliaga-Alcalde, G. Tobias, J. A. Ayllón and C. Domingo, Cryst. Growth Des., 2017, 17, 2864-2872.
- N. Portolés-Gil, S. Gowing, O. Vallcorba, C. Domingo, A. M. López- 59. Periago and J. A. Ayllón, J CO2 Util., 2018, 24, 444-453.
- 29. M. Kubovics, S. Rojas, A. M. López, J. Fraile, P. Horcajada and C. Domingo, J. Supercrit. Fluids, 2021, 178, 105379.
- 30. S. S.-Y. Chui, S. M.-F. Lo, J. P. H. Charmant, A. G. Orpen and I. D. Williams, Science, 1999, 283, 1148-1150.
- 31. J.-L. Zhuang, D. Ceglarek, S. Pethuraj and A. Terfort, Adv. Funct. Mater., 2011, 21, 1442-1447.
- 32. X. Mu, Y. Chen, E. Lester and T. Wu, Microporous Mesoporous Mater., 2018, 270, 249-257.
- 33. L. Guo, J. Du, C. Li, G. He and Y. Xiao, Fuel, 2021, 300, 120955.
- 34. C. H. Hendon and A. Walsh, Chem. Sci., 2015, 6, 3674-3683.
- 35. J. Panda, S. N. Sahu, R. Pati, P. K. Panda, B. C. Tripathy, S. K. Pattanayak and R. Sahu, ChemistrySelect, 2020, 5, 12398-12406.
- 36. L. Latifi and S. Sohrabnezhad, *Polyhedron*, 2020, **180**, 114321.
- 37. Q. Chen, Q.-W. Chen, C. Zhuang, P.-P. Tang, N. Lin and L.-Q. Wei, Inorg. Chem. Commun., 2017, 79, 78-81.
- 38. L. Yang, K. Wang, L. Guo, X. Hu and M. Zhou, J. Mater. Chem. B, 2024, **12**, 2670-2690.
- 39. L. Peng, J. Zhang, Z. Xue, B. Han, X. Sang, C. Liu and G. Yang, Nat. Commun., 2014, 5, 4465.
- 40. H. V. Doan, H. Amer Hamzah, P. Karikkethu Prabhakaran, C. Petrillo and V. P. Ting, Nanomicro Lett., 2019, 11, 54.
- 41. H. V. Doan, Y. Fang, B. Yao, Z. Dong, T. J. White, A. Sartbaeva, U. Hintermair and V. P. Ting, ACS Sustainable Chem. Eng., 2017, 5, 7887-7893.
- 42. R. Ameloot, E. Gobechiya, H. Uji-i, J. A. Martens, J. Hofkens, L. Alaerts, B. F. Sels and D. E. De Vos, Adv. Mater., 2010, 22, 2685-2688.
- 43. S.-D. Yeo, S.-J. Park, J.-W. Kim and J.-C. Kim, J. Chem. Eng. Data., 2000, 45, 932-935.
- 44. W. Wu, J. Ke and M. Poliakoff, J. Chem. Eng. Data., 2006, 51, 1398-
- 45. R. S. Chatwell, G. Guevara-Carrion, Y. Gaponenko, V. Shevtsova and J. Vrabec, Phys. Chem. Chem. Phys., 2021, 23, 3106-3115.
- 46. H. Pöhler and E. Kiran, J. Chem. Eng. Data., 1997, 42, 384-388.
- 47. S. Sima, V. Feroiu and D. Geană, J. Chem. Eng. Data., 2011, 56, 5052-5059.

- 2021, 549, 113201.
- 49. E. Lemmon, M. McLinden, D. Friend, P. Linstrom and W. Mallard, NIST standard reference database, 2011, 20899.
- chemistry webbook, NIST standard reference database, 2011.
- Data., 2018, 63, 2486-2499.
- 21. G. Sodeifian and M. M. B. Usefi, ChemBioEng Reviews, 2023, 10, 52. C. K. Zéberg-Mikkelsen, L. Lugo, J. García and J. Fernández, Fluid Phase Equilib., 2005, 235, 139-151.
- 22. H. Liu, B. Q. Chen, Y. J. Pan, C. P. Fu, R. K. Kankala, S. B. Wang and 53. B. Zhang, J. Zhang, C. Liu, X. Sang, L. Peng, X. Ma, T. Wu, B. Han and G. Yang, RSC Adv., 2015, 5, 37691-37696.
- 23. A. P. Nelson, O. K. Farha, K. L. Mulfort and J. T. Hupp, J. Am. Chem. 54. G. C. Bushell, Y. D. Yan, D. Woodfield, J. Raper and R. Amal, Adv. Colloid Interface Sci., 2002, 95, 1-50.
  - 55. M. Kumar, R. Li and J. D. Rimer, Chem. Mater., 2016, 28, 1714-1727.
  - A. A. Yakovenko, J. H. Reibenspies, N. Bhuvanesh and H.-C. Zhou, J. Appl. Crystallogr., 2013, 46, 346-353.
  - J. Cortés-Súarez, V. Celis-Arias, H. I. Beltrán, A. Tejeda-Cruz, I. A. Ibarra, J. E. Romero-Ibarra, E. Sánchez-González and S. Loera-Serna, ACS Omega, 2019, 4, 5275-5282.
  - D. Mustafa, E. Breynaert, S. R. Bajpe, J. A. Martens and C. E. A. Kirschhock, Chem. Commun., 2011, 47, 8037-8039.
  - 60. K. Schlichte, T. Kratzke and S. Kaskel, Microporous Mesoporous Mater., 2004, 73, 81-88.
  - 61. N. T. K. Thanh, N. Maclean and S. Mahiddine, Chem. Rev., 2014, **114**, 7610-7630.
  - 62. S. Karthika, T. K. Radhakrishnan and P. Kalaichelvi, Cryst. Growth Des., 2016, 16, 6663-6681.
  - 63. H. Fu, X. Gao, X. Zhang and L. Ling, Cryst. Growth Des., 2022, 22, 1476-1499.
  - 64. X. Liu, S. W. Chee, S. Raj, M. Sawczyk, P. Král and U. Mirsaidov, Proc. Natl. Acad. Sci., 2021, 118, e2008880118.
  - 65. J. I. Langford and A. J. C. Wilson, J. Appl. Crystallogr., 1978, 11, 102-113.
  - 66. B. Sun, S. Kayal and A. Chakraborty, *Energy*, 2014, **76**, 419-427.
  - 67. S. Gautam, J. Singhal, H. K. Lee and K. H. Chae, *Materials Today* Chemistry, 2022, 23, 100647.
  - 68. F. Caddeo, F. Himmelstein, B. Mahmoudi, A. M. Araújo-Cordero, D. Eberhart, H. Zhang, T. Lindenberg, A. Hähnel, C. Hagendorf and A. W. Maijenburg, Sci. Rep., 2023, 13, 13858.
  - 69. T. P. Vello, M. Strauss, C. A. R. Costa, C. C. Corrêa and C. C. Bof Bufon, Phys. Chem. Chem. Phys., 2020, 22, 5839-5846.
  - 70. P.-F. Hsieh, Z. X. Law, C.-H. Lin and D.-H. Tsai, Langmuir, 2022, 38, 4415-4424.
  - 71. J. Pich, S. K. Friedlander and F. S. Lai, J. Aerosol Sci., 1970, 1, 115-
  - 72. K. J. Ziegler, R. C. Doty, K. P. Johnston and B. A. Korgel, J. Am. Chem. Soc., 2001, 123, 7797-7803.
  - 73. L. Meli and P. F. Green, ACS Nano, 2008, 2, 1305-1312.
  - 74. A. L. Purohit, J. A. Misquith, B. R. Pinkard, S. J. Moore, J. C. Kramlich, P. G. Reinhall and I. V. Novosselov, Ind. Eng. Chem. Res., 2021, 60, 11458-11469.
  - 75. B. R. Pinkard, D. J. Gorman, E. G. Rasmussen, J. C. Kramlich, P. G. Reinhall and I. V. Novosselov, Int. J. Hydrogen Energy, 2019, 44, 31745-31756.
  - 76. B. R. Pinkard, J. C. Kramlich and I. V. Novosselov, ACS Sustainable Chem. Eng., 2020, 8, 4598-4605.
  - 77. J. Li, C. Austin, S. Moore, B. R. Pinkard and I. V. Novosselov, J. Chem. Eng., 2023, 451, 139063.

- 78. M. v. Smoluchowski, *Zeitschrift für Physikalische Chemie*, 1918, **92U**, 129-168.
- 79. P. Saffman and J. Turner, *J. Fluid Mech.*, 1956, **1**, 16-30.
- 80. K. P. Johnston and S. R. P. d. Rocha, *J. Supercrit. Fluids*, 2009, **47**, 523-530.
- 81. F. E. Kruis and K. A. Kusters, *Chem. Eng. Commun.*, 1997, **158**, 201-230.
- 82. J. Davis, E. Molnar and I. Novosselov, *Carbon*, 2020, **159**, 255-265.
- 83. J. Davis, K. Tiwari and I. Novosselov, Fuel, 2019, 245, 447-457.
- R. K. Chakrabarty, I. V. Novosselov, N. D. Beres, H. Moosmüller, C. M. Sorensen and C. B. Stipe, Appl. Phys. Lett., 2014, 104, 243103.

Page 11 of 11 Nanoscale

The authors confirm that the data supporting the findings of this study are available within the article and its supplementary materials.